

# An Augmented QCD Phase Portrait: Mapping Quark-Hadron Deconfinement for Hot, Dense, Rotating Matter under Magnetic Field

Gaurav Mukherjee<sup>a,b</sup>, D. Dutta<sup>a,b,\*</sup>, D. K. Mishra<sup>a</sup>

<sup>a</sup>Nuclear Physics Division, Bhabha Atomic Research Center, Mumbai 400085, India

<sup>b</sup>Homi Bhabha National Institute, Anushaktinagar, Mumbai - 400094, India

## Abstract

The quark-hadron transition that happens in ultra-relativistic heavy-ion collisions is expected to be influenced by the effects of rotation and magnetic field, both present due to the geometry of a generic non-head-on impact. We augment the conventional  $T-\mu_B$  planar phase diagram for QCD matter by extending it to a multi-dimensional domain spanned by temperature  $T$ , baryon chemical potential  $\mu_B$ , external magnetic field  $B$  and angular velocity  $\omega$ . Using two independent approaches, one from a rapid rise in entropy density and another dealing with a dip in the squared speed of sound, we identify deconfinement in the framework of a modified statistical hadronization model. We find that the deconfinement temperature  $T_C(\mu_B, \omega, eB)$  decreases nearly monotonically with increasing  $\mu_B$ ,  $\omega$  and  $eB$  with the most prominent drop (by nearly 40 to 50 MeV) in  $T_C$  occurring when all the three quasi-control (via collision energy and centrality) parameters are simultaneously tuned to finite values that are typically achievable in present and upcoming heavy-ion colliders.

**Keywords:** QCD phase diagram, Heavy-ion collisions, deconfinement, hadronic matter

**PACS:** 25.75.Gz, 12.38.Mh, 21.65.Qr, 25.75.-q, 25.75.Nq

## 1. Introduction

The beginning of this century marks the first experimental production and detection of quark-gluon plasma, an extreme phase of quantum chromodynamics (QCD), in ultra-relativistic heavy ion collisions (HIC) at the Relativistic Heavy Ion Collider (RHIC), BNL, and the Large Hadron Collider (LHC), CERN [1]. The same partonic matter is believed to have filled the early universe in its first microseconds after the Big Bang [2]. Upcoming facilities to further probe this exotic phase under varying conditions are under development, e.g., at Nuclotron-based Ion Collider fAcility (NICA), JINR, Dubna; the Facility for Antiproton and Ion Research (FAIR), GSI, Darmstadt; Heavy-Ion program at Japan Proton Accelerator Research Complex (JPARC-HI), Japan and High Intensity heavy-ion Accelerator Facility (HIAF), China.

Apart from very high temperatures and densities, the femto-scale system may also sustain significant rotation (parametrized by the angular velocity or vorticity  $\omega \approx (9 \pm 1) \times 10^{21} s^{-1} \sim 0.03 \text{ fm}^{-1} \sim 0.006 \text{ GeV}$  as experimentally discovered by the RHIC collaboration [3], higher theoretical estimates yield  $\omega \sim 0.1 \text{ fm}^{-1} \sim 0.02 \text{ GeV}$  [4, 5, 6]) and a strong magnetic field background ( $B \sim 10^{19}$  Gauss corresponding to  $eB \sim 6m_\pi^2 \sim 0.12 \text{ GeV}^2$  where  $e$  is the elementary charge and  $m_\pi$  is the pion mass [7, 8]) within the fireball droplet produced in a typical

off-central collision [9, 10, 11]. The extreme values of all these parameters (HIC fireballs are likely the hottest, densest, most vortical and embedded in the strongest magnetic fields, albeit briefly) are unique in the present-day universe. The only other conceivable physical situations that are qualitatively analogous might be the very early universe [12] and neutron star or magnetar cores [13] and even some quasi-relativistic condensed matter systems [14].

Thus a comprehensive treatment should include variables like angular velocity and magnetic field as additional parameters characterizing the hot and dense QCD matter. While certain effects of finite baryon chemical potential ( $\mu_B$ ), angular velocity ( $\omega$ ) and magnetic field ( $eB$ ), have been studied either separately or pairwise in the past, the interplay of all three and their combined impact on deconfinement and heavy-ion phenomenology seem to have been unexplored until now [11, 15, 16, 17]. The present work aims to advance in this direction by focusing on the rich phase structure of strongly interacting matter that manifests in the proposed multi-dimensional parameter space relevant for high-energy nucleus-nucleus collisions.

Here we adopt a modified hadron resonance gas (HRG) model, aka the statistical hadronization model [18, 19]. It is a unique tool for the kind of investigation of QCD matter that we need to make for the non-perturbative regime under study. The success of this model comes from accurately reproducing the particle abundances in HIC experiments [20]. Moreover, HRG results have been found to be in good agreement with lattice QCD simulations for temperatures upto the deconfinement temperature  $T_C$  [20, 21]. It also predicts the freeze-out points on the phase diagram that lie remarkably close to the deconfine-

\*Corresponding author

Email addresses: phy.res.gaurav.m@gmail.com (Gaurav Mukherjee), ddutta@barc.gov.in (D. Dutta), dkmishra@barc.gov.in (D. K. Mishra)

ment boundary for  $\mu_B$  upto and a little beyond 0.25 GeV where the so-called sign problem of lattice methods thwarts ab initio attempts [22]. The thermodynamic quantities computed in the model can be used to formulate criteria that we impose in order to locate, characterize and constrain the desired region where quark-hadron deconfinement occurs in the phase diagram, as will be elucidated below.

Deconfinement of hadronic matter when heated above a certain temperature range releases the quarks and gluons, the fundamental constituents of the theory. The resulting proliferation of the degrees of freedom in the system leads to a rapid increase in various thermodynamic quantities and this property when viewed in the Hagedorn picture gives us a means to estimate the deconfinement region in the phase diagram [23, 24]. The transition should also leave an imprint in the squared speed of sound [25] in the form of a prominent dip at the phase transition as may be intuitively expected given that it is essentially a ratio of the entropy density to the heat capacity and the latter diverges at a first-order phase transition.

In this Letter, we shall confine our investigation to the deconfinement (crossover) zone in the fully augmented QCD phase diagram for a parameter space that is most relevant for present and upcoming colliders (LHC, RHIC, NICA, FAIR). To accomplish this we are going to adopt two independent methods of estimating the deconfinement temperature both under the framework of the HRG model. Section 2 discusses the physical picture describing our system subjected to constraints and relations emerging from Landau quantization and relativistic causality. In Sec. 3, we begin with a formulation of the extended HRG model with parallel rotation and magnetic field followed by a computation of the required thermodynamic quantities. In Sec. 4, we discuss our strategy to study those characteristics that serve as excellent proxies for the onset of deconfinement and we selectively work with physical quantities that do not have a contribution from quantum zero-point (vacuum) fluctuations. Imposing a working criterion to extract the temperature of deconfinement, the entropy density will yield an estimate of the transition temperature. We will also study the speed of sound and impose a distinct condition from which another estimate for the deconfinement temperature may be obtained. In Sec. 5, we corroborate these results and discuss several implications. Finally, we summarize our findings and outline directions that may be studied further in the future in Sec. 6.

## 2. Landau quantization and causality bound under rotation

We consider a relativistic quantum gas rigidly rotating with angular velocity  $\vec{\omega}$  that is embedded in a uniform magnetic field  $\vec{B}$  and contained within a cylinder of radius  $R$  so that  $\vec{\omega} = (0, 0, \omega_z \equiv \omega)$  and  $\vec{B} = (0, 0, B_z \equiv B)$  are parallel. In such a system composed of both charged as well as neutral particles the former couple with the background magnetic field while the latter do not. To have a clear physical picture and disentangle the different influences let us first discuss just the magnetic coupling of a particle of charge  $Q$ . The well-known Landau levels,

$\varepsilon = \sqrt{p_z^2 + p_\perp^2 + m^2} = \sqrt{p_z^2 + |QB|(2n+1-2s_z) + m^2}$ , appear with degeneracy  $N = \lfloor \frac{|QB|S}{2\pi} \rfloor$  where  $S \sim R^2$  ( $S = \pi R^2$ , for our geometry) is the transverse area and  $n = 0, 1, 2, \dots$ . We should note here that  $p_\perp = \sqrt{|QB|(2n+1-2s_z)}$  is valid for both Dirac fermions with  $s_z = \pm 1/2$  [26] and scalar bosons [15]. We shall assume the same formula to hold true for particles of higher spin as well. Landau quantization dominates as long as  $N \gg 1$  or equivalently  $\frac{1}{\sqrt{|QB|}} \ll R$ , or in words,  $\frac{1}{\sqrt{|QB|}} \equiv l_B$ , the so-called magnetic length which is the characteristic length scale for the cyclotron orbits, should be sufficiently smaller than the system size,  $R = l_{\text{system}}$ . If  $l_{\text{system}} \lesssim l_B$ , the cyclotron motion is disturbed by the boundary and the degenerate Landau quantized spectra no longer apply. Thus when the caveat for Landau levels,  $(\frac{1}{\sqrt{|QB|}} = l_B) \ll R$  is violated (in the  $B = 0$  limit, say) the transverse momentum  $p_\perp$  becomes of order  $\frac{1}{R}$  (due to the edges) and not  $\frac{1}{l_B}$  [26]. We note that our work will employ Landau quantization and thus it strictly applies for sufficiently strong magnetic fields (or equivalently a large enough system size) relevant for HIC, unless otherwise mentioned.

Now, the introduction of a rigid, global rotation necessitates us to confine the system within a cylindrical boundary since at a distance  $r$  from the rotation axis, the azimuthal velocity,  $v = r\omega$ , should be below the vacuum speed of light,  $c = 1$ . This causality bound then mandates the system size to be below a threshold  $\frac{1}{\omega}$  which in turn provides an upper bound for the magnetic length  $l_B$  which has to be smaller than the system size  $R$  for Landau quantization to be valid [27]. This implies

$$1/\sqrt{|QB|} \ll R \leq 1/\omega. \quad (1)$$

The parameter space we shall study in this Letter falls within the bounds set by these inequalities. As a result, the  $B = 0$  substitution in our formulae for charged particles, for example the Landau quantized spectrum in  $\varepsilon$  and other relations introduced below, is not valid and separate formulae will be used for the neutral particles. Alternative approaches in the literature (see Refs. [15, 26, 28]) use a modified Landau spectrum in recognition of the distortion in the energy levels due to the boundary. This only becomes important when  $l_{\text{system}} \lesssim l_B$  which corresponds to a very narrow sliver ( $0 < eB \lesssim 0.0064 \text{ GeV}^2$  for  $l_B \sim l_{\text{system}} = 12.5 \text{ GeV}^{-1}$  or 2.5 fm) in the phase space that we will investigate. Also, these distortions occur due to the so-called edge states and become essentially irrelevant in the deep interior, i.e.,  $r \ll R$ , of the system where only the bulk states dominate [26, 28].

The phase space sum, required for the thermodynamic potential gets modified for the case of magnetic field (since for a fixed  $s_z$ ,  $p_\perp^2 = |QB|(2n+1-2s_z)$ ,  $dp_x dp_y \rightarrow 2\pi p_\perp dp_\perp = 2\pi|QB|dn$ ) to look like [27, 29]

$$\int \frac{dp_x dp_y}{(2\pi)^2} \rightarrow \frac{|QB|}{2\pi} \sum_{n=0}^{\infty} \quad (2)$$

and for rotation accompanying the magnetic field the Landau degeneracy ( $N = \frac{|QB|S}{2\pi}$  with  $S = \pi R^2$ ) is lifted by the canonical

orbital angular momentum quantum number  $l$  thus [27]

$$\int \frac{dp_x dp_y}{(2\pi)^2} \rightarrow \frac{1}{\pi R^2} \sum_{n=0}^{\infty} \sum_{l=-n}^{N-n} \quad (3)$$

These relations show a dimensional reduction of the phase space that effectively transforms  $\int d^3p$  to just  $\int dp_z$  and takes the particle dynamics from (3 + 1)-dimensions  $\rightarrow$  (1 + 1)-dimensions. The transverse phase plane  $\int 2\pi p_{\perp} dp_{\perp}$  collapses due to the discretization from Landau quantization and leaves only the longitudinal degree of freedom to be integrated over.

Under the constraints embodied in Eq. 1, we shall find that the complete dispersion relation for charged particles under  $\vec{\omega} \cdot \vec{B} > 0$  is given by Landau levels,  $\varepsilon = \sqrt{p_z^2 + |QB|(2n+1-2s_z) + m^2}$ , with an accompanying effective chemical potential induced by the rotation that lifts the Landau degeneracy, thus yielding  $\varepsilon \rightarrow \varepsilon - q\omega(l + s_z)$  where  $q = +1$  for the particle or positive charge state and  $q = -1$  for the anti particle or negative charge state [15, 27].

In the rest of this section we briefly review the calculations, explicitly performed in Ref. [27] for fermions and Ref. [15] for bosons, that support the formulae and arguments made above. Under the coordinate transformation suitable for a rigid global rotation, all local quantities can be expressed as functions of the co-rotating coordinates,  $x^{\mu}$ , in the non-inertial rotating frame of reference instead of  $\tilde{x}^{\mu}$  in the rest (lab) frame. The corresponding metric can be read as

$$g_{\mu\nu} = \eta_{ab} \frac{\partial \tilde{x}^a}{\partial x^{\mu}} \frac{\partial \tilde{x}^b}{\partial x^{\nu}} = \begin{pmatrix} 1 - (x^2 + y^2)\omega^2 & y\omega & -x\omega & 0 \\ y\omega & -1 & 0 & 0 \\ -x\omega & 0 & -1 & 0 \\ 0 & 0 & 0 & -1 \end{pmatrix}, \quad (4)$$

with the Minkowskian metric taken as  $\eta = \text{diag}(1, -1, -1, -1)$ . To deal with the fermions we introduce the vierbein,  $\eta_{ab} = e_a^{\mu} e_b^{\nu} g^{\mu\nu}$ , and adopt

$$e_0^t = e_1^x = e_2^y = e_3^z = 1, \quad e_0^x = y\omega, \quad e_0^y = -x\omega, \quad (5)$$

taking all other components zero.

The Dirac equation in a curved background space-time and gauge field is given by

$$[i\gamma^{\mu}(D_{\mu} + \Gamma_{\mu}) - m]\psi = 0, \quad (6)$$

where the covariant derivative is  $D_{\mu} \equiv \partial_{\mu} + iQA_{\mu}$ ,  $Q$  being the charge of the Dirac fermion. The  $\Gamma_{\mu}$  term is the usually defined affine connection associated with the rotating frame and containing Dirac spin matrices  $\sigma^{ij} = \frac{i}{2}[\gamma^i, \gamma^j]$ . Choosing the symmetric gauge  $A_{\mu} = (0, By/2, -Bx/2, 0)$ , we can have the explicitly written Dirac equation under parallel  $\vec{B}$  and  $\vec{\omega}$ .

$$[i\gamma^0(\partial_t - x\omega\partial_y + y\omega\partial_x - i\omega\sigma^{12}) + i\gamma^1(\partial_x + iQBy/2) + i\gamma^2(\partial_y - iQBx/2) + i\gamma^3\partial_z - m]\psi = 0 \quad (7)$$

We have already discussed the energy dispersion for spin  $s$  particles in a magnetic field at  $\omega = 0$ , given by

$$E^2 = p_z^2 + |QB|(2n+1-2s_z) + m^2 \quad (8)$$

with  $n = 0, 1, 2, \dots$ . We can separate out the contributions from rotation in Eq. 7 which are made of terms  $-i(\omega x\partial_y - \omega y\partial_x) + \omega\sigma^{12} = \omega(\hat{L}_z + \hat{S}_z)$ . If the eigenvalues of the  $\hat{L}_z$  and  $\hat{S}_z$  are denoted by  $l$  and  $s_z$  and from the recognition that  $E + \omega(l + s_z)$  is the energy eigenvalue in the inertial frame we arrive at

$$[E + \omega(l + s_z)]^2 = p_z^2 + |QB|(2n+1-2s_z) + m^2 \quad (9)$$

Thus the two branches of the energy eigenmodes  $E = \pm|E|$  corresponding to the particle and antiparticle states yield  $\sqrt{p_z^2 + |QB|(2n+1-2s_z) + m^2} \mp \omega(l + s_z)$  respectively. This result applies to spinless particles as well [15]. We now have all the ingredients (Eq. 3 and the above dispersion relation) to estimate the thermodynamic potential or free energy density [27, 30, 31] required for the HRG model formulation.

A physical picture reveals how the charged particles behave in a manner reminiscent of the classical Hall effect. The angular generalization ( $\phi = 0$  to  $2\pi$ ) of the linear Hall effect situation may be the mechanism via which a charge gradient or imbalance grows between the radially inner and outer regions of the circulating gas leading to a quasi-static or near-equilibrium system that can be legitimately treated in a statistically equilibrated ensemble for  $\omega \ll \sqrt{|QB|}$ .

We emphasize that as we are only interested in the bulk interior of the cylinder, the finite-size effects (due to edge states) are neglected in the calculations for the charged particles. For the regime that we operate in (strong magnetic field), there is negligible dependence on the local radial distance upto  $r \sim 0.8R$  since the edge states are localized near the boundary only [26, 28]. Schematically, a small magnetic length allows the system to accommodate ‘tight’ cyclotron orbits in the bulk that are intact from boundary interference. The opposite limit of large magnetic length ( $B \rightarrow 0$ ) lets the cyclotron orbits ‘loosen up’ (i.e., become less curved) and when they become comparable to the system size the boundary conditions become important. This implies that for the  $B = 0$  case we need to include the finite size effects and thus expect  $r$  dependence. We shall see this explicitly in the next section.

### 3. Statistical hadronization model with rotation and magnetic field

The composite ideal gas system in the HRG model consists of the charged baryons and mesons which are affected by the magnetic field (via Landau quantization) as well as the neutral particles that are not, if we neglect their anomalous magnetic moments. The corresponding thermodynamic formulae governing the charged and neutral particles thus look different as shown below.

The free energy density with the vacuum term suppressed for charged baryons and mesons, as discussed in the previous section, is expressed as

$$f_{i,c}^{b/m} = \mp \frac{T}{\pi R^2} \int \frac{dp_z}{2\pi} \sum_{n=0}^{\infty} \sum_{l=-n}^{N-n} \sum_{s_z=-s_i}^{s_i} \ln(1 \pm e^{-(\varepsilon_{i,c} - q_i\omega(l+s_z) - \mu_i)/T}), \quad (10)$$

where the dispersion relation contains the Landau levels

$$\varepsilon_{i,c} = \sqrt{p_z^2 + m_i^2 + |Q_i B|(2n - 2s_z + 1)}. \quad (11)$$

This obeys the constraint in Eq. 1 as we use undistorted Landau levels. The free energy density for the neutral particles [16] is given by

$$f_{i,n}^{b/m} = \mp \frac{T}{8\pi^2} \int_{(\Lambda_l^{\text{IR}})^2} dp_r^2 \int dp_z \sum_{l=-\infty}^{\infty} \sum_{\nu=l}^{l+2s_i} J_\nu^2(p_r r) \times \ln(1 \pm e^{-(\varepsilon_{i,n} - (l+s_i)\omega - \mu_i)/T}), \quad (12)$$

where the free part of the energy dispersion is given by

$$\varepsilon_{i,n} = \sqrt{p_r^2 + p_z^2 + m_i^2}. \quad (13)$$

Here  $Q_i$ ,  $q_i = Q_i/|Q_i|$ ,  $s_i$  and  $m_i$  are the charge, sign of charge, spin and mass of the  $i^{\text{th}}$  hadron and the subscripts  $c$  and  $n$  refer to charged particles and neutral particles respectively. The upper (lower) signs correspond to the baryons (mesons) as denoted by the superscript  $b$  ( $m$ ). The chemical potential  $\mu_i = Q_{B,i}\mu_B + Q_{e,i}\mu_e + Q_{S,i}\mu_S$  reflects the baryonic, electric charge and strangeness components of the  $i^{\text{th}}$  particle. We have set  $\mu_e = 0$  and  $\mu_S = 0$  here for simplicity and shall report the consequences of charge conservation and zero net-strangeness conditions in succeeding works.

In Eq. 10, the Landau degeneracy is lifted by rotation and the degenerate quantum number is the canonical orbital angular momentum  $l$ . The summation  $\sum_{l=-n}^{N-n}$  over  $l$  runs upto  $N - n$ . Since  $N$  is a function of the magnetic field, differentiation of the free energy density with respect to the magnetic field requires us to take this into account. Similarly, in Eq. 12, there is an  $\omega$ -dependent infrared cutoff ( $\Lambda_l^{\text{IR}}$ ) in the  $p_r$  integration  $\int_{\Lambda_l^{\text{IR}}} dp_r^2$ , where  $\Lambda_l^{\text{IR}} = \xi_{l,1}\omega$  and  $\xi_{l,1}$  is the first zero of the Bessel function.

We now comment on the conspicuous presence of the transverse phase space and configuration space coordinates  $p_r$  or  $p_\perp$  and  $r$  in Eq. 12. As explained in Sec. 2, both of these are expected for the neutral particles which are insensitive to the magnetic field. Their trajectories are thus strongly affected by the centrifugation effect due to rotation and the finite boundary. This is not the case for Eq. 10 when the magnetic field is large enough. More specifically, the dimensional reduction of phase space from Landau quantization (Eqs. 2,3) leaves only  $\int dp_z$  in Eq. 10 whereas for the  $B = 0$  case in Eq. 12,  $\int dp_r^2$  is retained.

If we had included boundary effects for  $B \neq 0$  (as done in Ref. [26] for  $\omega = 0$ ), we would have  $\varepsilon = \sqrt{p_z^2 + 2|QB|\lambda_{l,k} + m^2}$  (instead of  $\sqrt{p_z^2 + 2|QB|n + m^2}$  for spin up), where  $\lambda_{l,k}$  represents a modified Landau level index in a finite-size system and its explicit form depends on the boundary condition at  $r = R$ . With an imposed boundary the Landau wavefunction is also deformed by the finite-size effect and contains the confluent hypergeometric function. These wavefunctions  $\Phi_l$  and  $\Phi_{l+1}$  in that case reduce to Bessel functions in the limit  $B \rightarrow 0$ , i.e.,  $\Phi_l(\lambda_{l,k}, \frac{|QB|r^2}{2}) \rightarrow J_l(\sqrt{2|QB|\lambda_{l,k}r})$  and  $\Phi_{l+1}(\lambda_{l,k} - 1, \frac{|QB|r^2}{2}) \rightarrow J_{l+1}(\sqrt{2|QB|\lambda_{l,k}r})$ . We identify the argument  $\sqrt{2|QB|\lambda_{l,k}r}$  with

$p_\perp r = p_r r$ . This justifies the appearance of the Bessel functions in Eq. 12 where boundary effects are accounted for.

There is no counterpart in Eq. 10 of the Bessel functions in Eq. 12 on account of the following reason. In Eq. 12 we work in cylindrical coordinates since it is the natural formulation suited to the geometry of the system, and the Bessel function arises from the weight in the Bessel-Fourier expansion. However, in a magnetic field obeying Eq. 1 the dimensional reduction in Eq. 3 encapsulates the transverse phase plane and thus  $p_r$  disappears in Eq. 10 along with the  $J_\nu^2(p_r r)$  part. A possible justification for this may be that the wave-function should be exponentially localized around the axis ( $r = 0$ ) for large  $eB$ , and the Bessel function part could be approximated by unity at  $r = 0$ .

We note that in our approximation Eq. 12 is not recoverable from Eq. 10 under the substitution  $B = 0$  simply because  $B$  is not a small perturbation (no weak field limit  $B \rightarrow 0$  exists) in Eq. 10, in light of the constraint in the first inequality in Eq. 1. We remark that this kind of a disconnected  $B = 0$  and strong  $B \neq 0$  treatment applied to the HRG model has already been successfully employed in the literature (see Refs. [11, 29, 32, 33]).

We have taken fixed values of  $r = 3 \text{ GeV}^{-1}$  and  $R = 12.5 \text{ GeV}^{-1}$  (or  $R = 2.5 \text{ fm}$ ,  $\sim$  system radius for peripheral collisions at freeze-out [34]), so as to have definite, unambiguous results valid for our idealized system. Since our principal aim here is to explore the phase structure, we bypass a thorough study of the radial dependence and possible inhomogeneous equations of state [35].

For the system we are dealing with, the free energy density reads

$$f = \varepsilon - Ts - \mu_B n_B - \omega j - Bm_B = -p,$$

where pressure  $p$ , energy density  $\varepsilon$ , entropy density  $s$ , baryon number density  $n_B$ , magnetization  $m_B$  and total angular momentum  $j$  are the relevant observables. All the observables here satisfy simple differential relations,  $s = -\frac{\partial f}{\partial T}$ ,  $n_B = -\frac{\partial f}{\partial \mu_B}$ ,  $j = -\frac{\partial f}{\partial \omega}$ ,  $m_B = -\frac{\partial f}{\partial B}$ . It is required to use Leibniz rule to carry out differentiation of the free energy with respect to the angular velocity while computing the total angular momentum. The squared speed of sound is defined as  $c_s^2 = \frac{\partial p}{\partial \varepsilon}|_{(\mu_B, \omega, eB)} = \frac{\frac{\partial p}{\partial T}|_{(\mu_B, \omega, eB)}}{[\frac{\partial \varepsilon}{\partial T}|_{(\mu_B, \omega, eB)}]}$  and here comes out to be

$$c_s^2 = \frac{s}{\left(T \frac{\partial s}{\partial T} + B \frac{\partial m_B}{\partial T} + \omega \frac{\partial j}{\partial T} + \mu_B \frac{\partial n_B}{\partial T}\right)|_{(\mu_B, \omega, eB)}}. \quad (14)$$

All required thermodynamic quantities can be computed from the free energy density and plugged in to obtain the desired results.

All hadrons, upto a mass of 1.5 GeV and excluding those having spin-3/2, listed in the particle data group list of particles contained in the package of THERMUS-V3.0 [36] have been included in our HRG model treatment. The ultraviolet mass cut-off is taken to reduce numerical cost and the exclusion of the spin-3/2 sector has been implemented due an instability in its theory [29, 37, 38, 39].

#### 4. Strategy to identify deconfinement

The first criterion that we employ to characterize the deconfinement transition and demarcate its location on the multi-dimensional QCD phase diagram is based on an argument regarding the physical reinterpretation of the Hagedorn limiting temperature concept [23, 40]. Historically, the original interpretation of the Hagedorn temperature as a limiting temperature within the hadronic bootstrap model framework was revised [41] when it was realized that the same should be construed as the transition temperature to more fundamental degrees of freedom, namely the quarks and gluons. A drastic rise in thermodynamic quantities like the entropy density is expected during the deconfinement transition. Since this transition is of crossover type, we do not see a strict discontinuity or divergence but rather a sharp change within a narrow temperature window. We choose a working condition for deconfinement along these lines [16, 24]. From an experimental standpoint too there is a strong indication that the hadro-chemical freeze-out curve determined by the so-called universal freeze-out conditions can act as a close proxy for the deconfinement band region in the phase diagram, and this is most accurate in the small to medium baryo-chemical potential range [22].

Another pragmatic way to deduce the onset of deconfinement involves the speed of sound which has been studied to distinguish QCD phases in highly varied contexts [42, 43]. In contrast to the somewhat arbitrary condition imposed on the scaled entropy density to reach the  $T_C$  estimate, the dip in the squared speed of sound,  $c_s^2$  provides precise values for  $T_C$  independently [44]. If the phase transition were strictly first-order then we would have expected a discontinuity at  $T = T_C$  where  $c_s^2$  should vanish [25]. The crossover nature of the quark-hadron transition leads to the relatively smooth and shallow minima of  $c_s^2$  occurring at and near the deconfinement as seen in Fig. 1. We shall now extend the evaluation of these observables to new regimes in parameter space using the generalized HRG model as detailed above. Extrapolating the validity of the conditions for deconfinement, we will be able to map out the QCD phases in a multi-dimensional domain.

#### 5. Results and discussion

We compute the entropy density numerically and impose the criteria  $s/T^3 = 4 - 7$  to constrain the range within which the deconfinement transition occurs most dramatically (rapid rise in thermodynamic quantities). This leads to the deconfinement bands shown in Fig. 2 for the scenarios without ( $eB = 0$ ) and with ( $eB = 0.15 \text{ GeV}^2$ ) magnetic field. We have taken  $\mu_e = 0$  and  $\mu_s = 0$  for simplicity. We observe a successive lowering of the deconfinement crossover zone due to finite magnetic field as  $\omega$  rises from 0 to 0.02 GeV ( $\sim 3 \times 10^{22} \text{ s}^{-1}$ ). The trend is clear across the span of these external parameters: the dip in  $T_C$  is amplified substantially when both the magnetic field and the angular velocity take on high values and at the baryon chemical potential of around 0.5 GeV, the drop reaches a nadir nearing 0.1 GeV. This is remarkable since at zero magnetic field the effect of rotation with  $\omega$  rising from 0 to 0.02 GeV is only slight

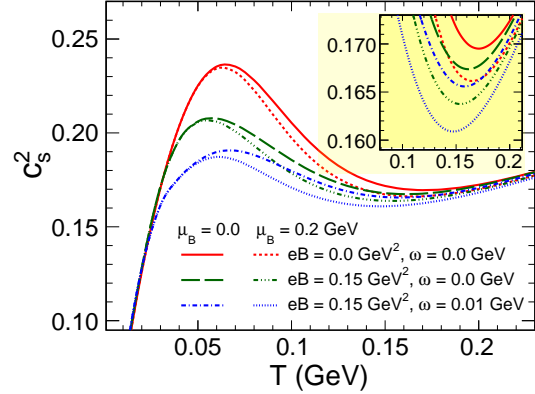


Figure 1: The variation of the squared speed of sound as a function of temperature with a magnified view of the region where the minima occur in the inset.

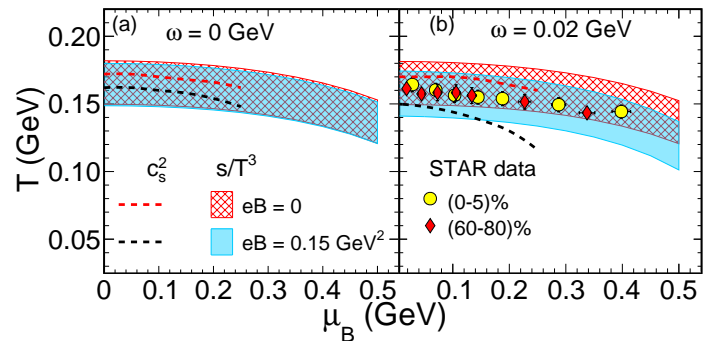


Figure 2: QCD phase diagrams,  $T$  vs.  $\mu_B$  for  $eB = 0$  (red band or curve) and  $eB = 0.15 \text{ GeV}^2$  (blue band or curve) and (a) for  $\omega = 0 \text{ GeV}$  and (b) for  $\omega = 0.02 \text{ GeV}$ . The deconfinement transition zones depicted as (i) bands constrained by  $s/T^3 = 4$  (lower edge) and 7 (upper edge), and (ii) curves obtained from the minima of  $c_s^2$  vs.  $T$  as shown in Fig. 1.

within the range considered here. However the simultaneous imposition of an external magnetic field over and above the rotation leads to nearly the same drop in the deconfinement temperature at  $\omega = 0.02 \text{ GeV}$  as that estimated at extremely large values of  $\omega = 0.3 \text{ GeV}$  when there is no magnetic field present at all [16]. This would suggest that although the latter (pure,  $eB = 0$ ) rapid rotation scenario might be too high for a typical HIC at the time of deconfinement and chemical freeze-out, a similar (in magnitude) effective downward shift of the deconfinement temperature may nevertheless still apply if the realistic situation sustains a strong enough magnetic field ( $eB \sim 0.12 \text{ GeV}^2$  [7]) accompanying the more modest but also more plausible  $\omega$  values ( $\sim 0.02 \text{ GeV}$ , [3, 4, 5, 6]) as in the case of the former which has been examined in the current study. As the QGP droplet produced in a HIC (particularly those with finite  $\mu_B$ ,  $\omega$  and  $eB$ ) evolves from its initial formation to hadronization, the pronounced lowering of  $T_C$  may lead to a longer lifetime for the deconfined phase.

In Fig. 2, we have also shown data points for chemical freeze-out [34] as extracted from experimental particle yields and ratios for two centrality classes, (0-5)% and (60-80)%. When such fitting analyses incorporate rotation and magnetic field as addi-

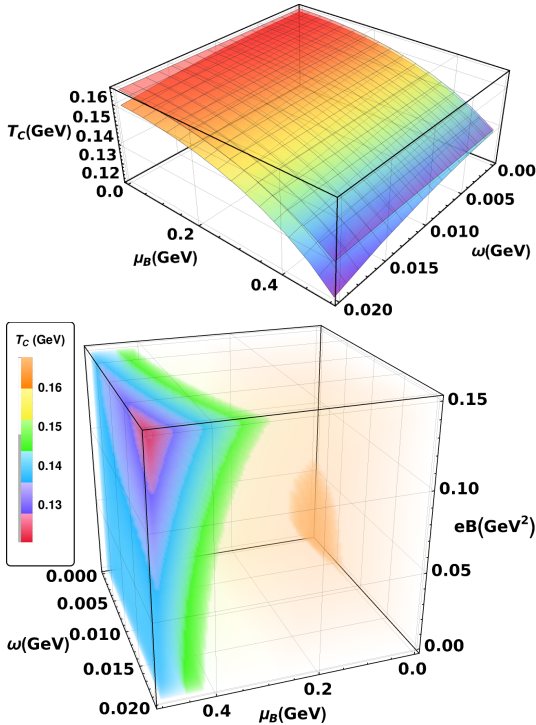


Figure 3: (Top) Deconfinement transition surfaces showing  $T_C(\mu_B, \omega)$  for  $eB = 0$  (upper surface) and  $eB = 0.15 \text{ GeV}^2$  (lower surface). (Bottom) Augmented phase diagram showing  $T_C(\mu_B, \omega, eB)$  as a color-coded density plot where the  $T_C$ -calibrated legend (left) provides reference for the different iso- $T_C$  contour boundaries in the  $\mu_B, \omega, eB$  space. Both plots obtained from rapid rise in entropy density at  $s/T^3 = 5.5$ .

tional quasi-control parameters ( $\mu_B, \omega$  and  $eB$ , all dependent on collision energy and impact parameter or centrality), our phenomenological results may be better interpreted. The comparison might lead to not only  $T - \mu_B$  freeze-out data serving as ‘thermometer’ and ‘baryometer’ [18] but also possibly augment them with capabilities of ‘magnetometer’ [11] and ‘anemometer’ to estimate the magnitudes of magnetic field and rotational motion prevalent in a HIC fireball. The degree of the relative influences of  $\mu_B, \omega$  and  $eB$  might be constrained from other observable phenomena, for example measured polarization [3] to independently constrain  $\omega$ , etc.

Since we now have  $T_C(\mu_B, \omega, eB)$ , that is the deconfinement temperature estimate as a function of three independent parameters, we can depict the variation of  $T_C$  in higher dimensional spaces to visually understand the individual and combined effects of  $\mu_B, \omega$  and  $eB$  on  $T_C$ . Top panel of Fig. 3 shows the surface plots (3-D QCD phase diagram)  $T_C(\mu_B, \omega)$  for  $eB = 0$  and  $eB = 0.15 \text{ GeV}^2$ . The values of  $T_C$  on each surface are obtained from the rapid rise condition of scaled entropy density,  $s/T^3 = 5.5$ . This particular value of the scaled entropy density is found to sit roughly midway within the deconfinement bands depicted in Fig. 2. This also leads to a close correspondence in the variation of  $T_C$  vs.  $\mu_B$  as compared with the parallel analysis made using the minima of the squared speed of sound. The lowering of the  $T_C$  vs.  $\mu_B$  curve due to the imposed magnetic field of  $eB = 0.15 \text{ GeV}^2$  is seen to be progressively

amplified as we crank up  $\omega$  from 0 to 0.02 GeV. An even more fine-grained data set is next exhibited in the (4-D QCD phase diagram)  $T_C(\mu_B, \omega, eB)$  density plot in the bottom panel of Fig. 3. The diagram shows a detailed view of the initial gradual  $T_C$  change near the origin at  $(\mu_B, \omega, eB) = (0, 0, 0)$  as the independent variables rise from 0 values and the rapid drop in  $T_C$  when the three attain higher values near the diagonally opposite corner where isotherms (constant  $T_C$  contours) take shape and pile up in layered or stratified form. These phase portraits, from the discrete curves, bands and surfaces (2-D and 3-D) to the continuous density plots (4-D) help us visualize the  $T_C$  dependence on increasing  $\mu_B, \omega$  and  $eB$  in the experimentally interesting parameter space chosen here.

We also reach an independent estimate for the deconfinement temperature by utilizing the squared speed of sound which, like the entropy density, is a quantity that is insensitive to any vacuum term contribution and can be computed from the modified HRG model. A dip in the squared speed of sound,  $c_s^2$ , reveals the softest point in the equation-of-state and signals a phase transition. Thus the locations of the minima should serve as a faithful proxy for the onset of deconfinement. We exploit this property to obtain an independent prediction of the deconfinement region within the QCD phase diagram. Figure 2 superposes the  $T_C$  curves obtained from the  $c_s^2$  minima onto the results obtained from the Hagedorn limiting temperature condition on the entropy density. Both methods lead to the conclusion that the drop in  $T_C$  is strongly enhanced at high  $\mu_B, \omega$  and  $eB$ .

Figure 4 shows the  $T_C$  values obtained from the speed of sound analysis and these results are analogous to the results shown in Fig. 3. In our investigations of the squared speed of sound, the observed dip becomes shallower [43, 45] and shows smearing as  $\mu_B$  or  $\omega$  or  $eB$  rise. We also notice that the drop in  $T_C$  obtained from the entropy density analysis is somewhat smaller than that from the speed of sound analysis. A similar trend, namely the dip in the squared speed of sound being more sensitive (to the magnetic field) than the entropy density, was observed in Ref. [29] also. An exact quantitative correspondence is not expected anyway between the results from the two distinct methods and thus the obtained pseudo-critical temperatures (no unique  $T_C$  for a non-singular crossover [46]) serve as an approximate determination of a continuous transition. The ambiguity of precisely where the deconfinement curve/surface cuts the  $T$  axis notwithstanding, we infer that the augmented HRG model predicts a decrease in  $T_C$  (by a maximum of 40 to 50 MeV in the parameter ranges considered here) as we venture into the (non-zero  $T, \mu_B, \omega, eB$ ) hinterland of the augmented QCD phase space.

We now discuss the physics motivations behind taking two distinct routes. Firstly, since there is no treatment in the literature, to the best of our knowledge, that studies the non-perturbative QCD thermodynamics and phase structure under simultaneously non-zero  $\omega, \mu_B$  and  $eB$ , it is important to cross-check the results we obtain by confirming that our two different approaches are mutually validated. If the results obtained by constraining  $s/T^3$  (invoking the Hagedorn argument) are corroborated qualitatively and even quantitatively to close proxim-

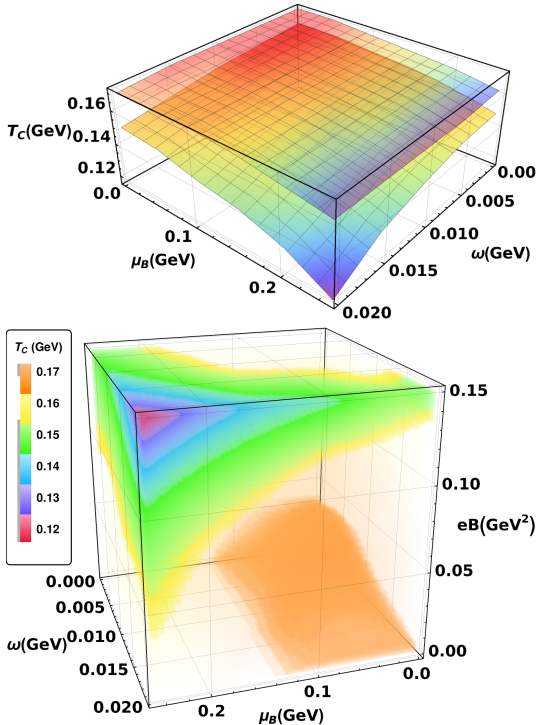


Figure 4: (Top) Deconfinement transition surfaces showing  $T_C(\mu_B, \omega)$  for  $eB = 0$  (upper surface) and  $eB = 0.15 \text{ GeV}^2$  (lower surface). (Bottom) Augmented phase diagram showing  $T_C(\mu_B, \omega, eB)$  as a color-coded density plot where the  $T_C$ -calibrated legend (left) provides reference for the different iso- $T_C$  contour boundaries in the  $\mu_B, \omega, eB$  space. Both obtained from the minima of the squared speed of sound.

ity with an independent method, like minimizing  $c_s^2$ , one can be confident that the consistent results from these methods constitute a robust and novel prediction of the augmented HRG model. Thus our twin approach serves to substantiate the basic results found. Again, the choice of  $s/T^3$  and  $c_s^2$  over other criteria like scaled  $p$  [16] and  $n$  [24],  $\epsilon/n$  [11, 33],  $n_B + n_{\bar{B}}$  [33] lets us bypass the vacuum term ( $T = 0$ ) that would otherwise require renormalization [29]. Also,  $c_s^2$  as computed in the generalized HRG model treated here opens up the possibility of going beyond studying just the freeze-out stage thermodynamics to also matching with the hydrodynamics of the QGP phase. Our evaluation of  $c_s^2$ , being a key ingredient in hydrodynamic calculations, fireball evolution, elliptic flow studies, conformal symmetry breaking in hot QCD, etc. [25] will serve as a starting point for more detailed studies in forthcoming work.

We discuss the HIC phenomenological aspects with regard to the ‘magnetometer’ and ‘anemometer’ measurability proposal. Let us denote by ‘x’ the control parameters (like collision energy, centrality, rapidity) that can be adjusted to vary the  $\mu_B, \omega$  and  $eB$  at which the system crosses the transition region [47]. The existing parameterization for chemical freeze-out data seems well-suited to be extended to include  $\omega, eB$  along with  $T$  and  $\mu_B$ . The universal freeze-out condition,  $s/T^3 \sim 7$  [48], can be tested thereafter in the extrapolated phase space by comparing with  $T - \mu_B$  data for varying centrality, collision energy and rapidity. The  $c_s^2$  minima are more directly

associated with QCD phase transitions, particularly the deconfinement boundary [25]. There is strong evidence that the deconfinement boundary and chemical freeze-out line merge for small  $\mu_B$ . This is supported by the common and close trend found in our results in Fig. 3 and Fig. 4. The quantitative differences between Fig. 3 and Fig. 4 will probably help in the quite non-trivial task of disentangling or segregating the individual contributions of  $\mu_B, \omega$  and  $eB$  to the convoluted processes within a hadronizing HIC droplet. Perhaps some additional refinements in modeling the actual fireball system more realistically will provide further fine-tuning of the results in the future.

It is interesting to note that certain aspects of the chiral transition explored in the literature [49, 50] share similarities to the deconfinement transition which has been the focus of our study here. The inverse magnetic catalysis (IMC) leads to a decrease in the chiral transition temperature with an increasing magnetic field in the presence of non-zero chemical potential and also some other influences [51, 52, 53, 54]. Observing that rotation induces an effective chemical potential, a phenomenon analogous to inverse magnetic catalysis called rotational magnetic inhibition [27] or inverse magnetorotational catalysis (IMRC) [55] was proposed. It is conceivable that the common decreasing trend expected for the critical temperature in these studies involving, in each case, only two of the three independent variables  $\mu_B, \omega, eB$ , gets reinforcement when all of the three are present simultaneously. This work may shed some light on whether the two transition temperatures stay locked in value or split as we turn on the various parameters to finite values and advance into the (augmented) phase diagram interior.

## 6. Summary

We set out to examine the deconfinement zone of the QCD phase diagram for hot and dense matter that is subjected to an external magnetic field and a parallel global rotation as might be present in a typical non-central heavy-ion collision. For this we utilized the HRG model with suitable modifications due to the additional parameters of magnetic field and angular velocity. We calculated the entropy density and squared velocity of sound as functions of temperature. We showed, based on our imposed criteria for the identification of deconfinement, that the simultaneous turning on of both the magnetic field and angular velocity appears to significantly amplify the drop in  $T_C$  due to baryon-chemical potential even further, by close to 40 to 50 MeV. We observed that the decrease of  $T_C$  for HIC values of  $\mu_B, \omega$  and  $eB$  is substantial and comparable to that due to the much higher but experimentally implausible  $eB$  or  $\omega$  values if considered separately. One potential application is the possibility of accessing the HIC fireball properties by using this approach as a ‘thermometer’, ‘baryometer’, ‘magnetometer’ and ‘anemometer’-like tool. We also discussed a possible extension of the lifetime of the QGP phase in HIC, the deconfinement and chiral transitions in our new regime and speculated about their correspondence, i.e., splitting versus locking. The direction of research pursued here, incorporating the combined effects of  $\mu_B, \omega$  and  $eB$ , opens up new avenues for future explorations

into uncharted QCD phase territory, in tandem with present and upcoming heavy-ion colliders.

**Acknowledgments** The authors thank A. K. Mohanty for valuable feedback and discussions. We also gratefully acknowledge the anonymous referee whose insightful suggestions led to overall improvement of this work.

## References

- [1] A. Bzdak, S. Esumi, V. Koch, J. Liao, M. Stephanov, N. Xu, Mapping the Phases of Quantum Chromodynamics with Beam Energy Scan, *Phys. Rept.* 853 (2020) 1–87. [arXiv:1906.00936](#), [doi:10.1016/j.physrep.2020.01.005](#).
- [2] D. H. Rischke, The Quark gluon plasma in equilibrium, *Prog. Part. Nucl. Phys.* 52 (2004) 197–296. [arXiv:nucl-th/0305030](#), [doi:10.1016/j.pnpnp.2003.09.002](#).
- [3] L. Adamczyk, et al., Global  $\Lambda$  hyperon polarization in nuclear collisions: evidence for the most vortical fluid, *Nature* 548 (2017) 62–65. [arXiv:1701.06657](#), [doi:10.1038/nature23004](#).
- [4] F. Becattini, G. Inghirami, V. Rolando, A. Beraudo, L. Del Zanna, A. De Pace, M. Nardi, G. Pagliara, V. Chandra, A study of vorticity formation in high energy nuclear collisions, *Eur. Phys. J. C* 75 (9) (2015) 406, [Erratum: *Eur.Phys.J.C* 78, 354 (2018)]. [arXiv:1501.04468](#), [doi:10.1140/epjc/s10052-015-3624-1](#).
- [5] Y. Jiang, Z.-W. Lin, J. Liao, Rotating quark-gluon plasma in relativistic heavy ion collisions, *Phys. Rev. C* 94 (4) (2016) 044910, [Erratum: *Phys.Rev.C* 95, 049904 (2017)]. [arXiv:1602.06580](#), [doi:10.1103/PhysRevC.94.044910](#).
- [6] W.-T. Deng, X.-G. Huang, Vorticity in Heavy-Ion Collisions, *Phys. Rev. C* 93 (6) (2016) 064907. [arXiv:1603.06117](#), [doi:10.1103/PhysRevC.93.064907](#).
- [7] D. E. Kharzeev, L. D. McLerran, H. J. Warringa, The Effects of topological charge change in heavy ion collisions: 'Event by event P and CP violation', *Nucl. Phys. A* 803 (2008) 227–253. [arXiv:0711.0950](#), [doi:10.1016/j.nuclphysa.2008.02.298](#).
- [8] W.-T. Deng, X.-G. Huang, Event by Event generation of electromagnetic fields in heavy-ion collisions, *Phys. Rev. C* 85 (2012) 044907. [arXiv:1201.5108](#), [doi:10.1103/PhysRevC.85.044907](#).
- [9] X.-G. Huang, Electromagnetic fields and anomalous transports in heavy-ion-collisions—a pedagogical review, *Rep. Prog. Phys.* 79 (2016) 076302. [doi:10.1088/0034-4885/79/7/076302](#).
- [10] F. Becattini, M. A. Lisa, Polarization and Vorticity in the Quark–Gluon Plasma, *Ann. Rev. Nucl. Part. Sci.* 70 (2020) 395–423. [arXiv:2003.03640](#), [doi:10.1146/annurev-nucl-021920-095245](#).
- [11] K. Fukushima, Y. Hidaka, Magnetic Shift of the Chemical Freeze-out and Electric Charge Fluctuations, *Phys. Rev. Lett.* 117 (10) (2016) 102301. [arXiv:1605.01912](#), [doi:10.1103/PhysRevLett.117.102301](#).
- [12] B. Cheng, A. V. Olinto, Primordial magnetic fields generated in the quark-hadron transition, *Phys. Rev. D* 50 (1994) 2421–2424. [doi:10.1103/PhysRevD.50.2421](#).
- [13] M. G. Alford, A. Schmitt, K. Rajagopal, T. Schäfer, Color superconductivity in dense quark matter, *Rev. Mod. Phys.* 80 (2008) 1455–1515. [arXiv:0709.4635](#), [doi:10.1103/RevModPhys.80.1455](#).
- [14] V. A. Miransky, I. A. Shovkova, Quantum field theory in a magnetic field: From quantum chromodynamics to graphene and Dirac semimetals, *Phys. Rept.* 576 (2015) 1–209. [arXiv:1503.00732](#), [doi:10.1016/j.physrep.2015.02.003](#).
- [15] Y. Liu, I. Zahed, Pion Condensation by Rotation in a Magnetic field, *Phys. Rev. Lett.* 120 (3) (2018) 032001. [arXiv:1711.08354](#), [doi:10.1103/PhysRevLett.120.032001](#).
- [16] Y. Fujimoto, K. Fukushima, Y. Hidaka, Deconfining Phase Boundary of Rapidly Rotating Hot and Dense Matter and Analysis of Moment of Inertia, *Phys. Lett. B* 816 (2021) 136184. [arXiv:2101.09173](#), [doi:10.1016/j.physletb.2021.136184](#).
- [17] Y. Jiang, J. Liao, Pairing Phase Transitions of Matter under Rotation, *Phys. Rev. Lett.* 117 (19) (2016) 192302. [arXiv:1606.03808](#), [doi:10.1103/PhysRevLett.117.192302](#).
- [18] A. Andronic, P. Braun-Munzinger, K. Redlich, J. Stachel, Decoding the phase structure of QCD via particle production at high energy, *Nature* 561 (2018) 321–330. [arXiv:1710.09425](#), [doi:10.1038/s41586-018-0491-6](#).
- [19] P. Garg, D. K. Mishra, P. K. Netrakanti, B. Mohanty, A. K. Mohanty, B. K. Singh, N. Xu, Conserved number fluctuations in a hadron resonance gas model, *Phys. Lett. B* 726 (2013) 691–696. [arXiv:1304.7133](#), [doi:10.1016/j.physletb.2013.09.019](#).
- [20] A. Andronic, P. Braun-Munzinger, J. Stachel, M. Winn, Interacting hadron resonance gas meets lattice QCD, *Phys. Lett. B* 718 (2012) 80–85. [arXiv:1201.0693](#), [doi:10.1016/j.physletb.2012.10.001](#).
- [21] A. Tawfik, QCD phase diagram: A Comparison of lattice and hadron resonance gas model calculations, *Phys. Rev. D* 71 (2005) 054502. [arXiv:hep-ph/0412336](#), [doi:10.1103/PhysRevD.71.054502](#).
- [22] Z. Fodor, S. D. Katz, Critical point of QCD at finite T and  $\mu$ , lattice results for physical quark masses, *JHEP* 04 (2004) 050. [arXiv:hep-lat/0402006](#), [doi:10.1088/1126-6708/2004/04/050](#).
- [23] R. Hagedorn, Statistical thermodynamics of strong interactions at high-energies, *Nuovo Cim. Suppl.* 3 (1965) 147–186.
- [24] K. Fukushima, Phase diagram of hot and dense QCD constrained by the Statistical Model, *Phys. Lett. B* 695 (2011) 387–391. [arXiv:1006.2596](#), [doi:10.1016/j.physletb.2010.11.040](#).
- [25] Z. V. Khaidukov, M. S. Lukashov, Y. A. Simonov, Speed of sound in the QGP and an SU(3) Yang-Mills theory, *Phys. Rev. D* 98 (7) (2018) 074031. [arXiv:1806.09407](#), [doi:10.1103/PhysRevD.98.074031](#).
- [26] H.-L. Chen, K. Fukushima, X.-G. Huang, K. Mameda, Surface Magnetic Catalysis, *Phys. Rev. D* 96 (5) (2017) 054032. [arXiv:1707.09130](#), [doi:10.1103/PhysRevD.96.054032](#).
- [27] H.-L. Chen, K. Fukushima, X.-G. Huang, K. Mameda, Analogy between rotation and density for Dirac fermions in a magnetic field, *Phys. Rev. D* 93 (10) (2016) 104052. [arXiv:1512.08974](#), [doi:10.1103/PhysRevD.93.104052](#).
- [28] M. N. Chernodub, S. Gongyo, Edge states and thermodynamics of rotating relativistic fermions under magnetic field, *Phys. Rev. D* 96 (2017) 096014. [doi:10.1103/PhysRevD.96.096014](#). URL <https://link.aps.org/doi/10.1103/PhysRevD.96.096014>
- [29] G. Endrödi, QCD equation of state at nonzero magnetic fields in the Hadron Resonance Gas model, *JHEP* 04 (2013) 023. [arXiv:1301.1307](#), [doi:10.1007/JHEP04\(2013\)023](#).
- [30] S. Ebihara, K. Fukushima, K. Mameda, Boundary effects and gapped dispersion in rotating fermionic matter, *Phys. Lett. B* 764 (2017) 94–99. [arXiv:1608.00336](#), [doi:10.1016/j.physletb.2016.11.010](#).
- [31] G. Endrödi, [Lecture notes on thermal quantum field theory](#). URL <https://itp.uni-frankfurt.de/~endrodi/thermalFT.pdf>
- [32] A. Bhattacharyya, S. K. Ghosh, R. Ray, S. Samanta, Exploring effects of magnetic field on the hadron resonance gas, *Europhysics Letters* 115 (6) (2016) 62003. [doi:10.1209/0295-5075/115/62003](#). URL <https://dx.doi.org/10.1209/0295-5075/115/62003>
- [33] R. K. Mohapatra, Effect of inverse magnetic catalysis on conserved-charge fluctuations in a hadron resonance gas model, *Phys. Rev. C* 99 (2019) 024902. [doi:10.1103/PhysRevC.99.024902](#). URL <https://link.aps.org/doi/10.1103/PhysRevC.99.024902>
- [34] L. Adamczyk, et al., Bulk properties of the medium produced in relativistic heavy-ion collisions from the beam energy scan program, *Phys. Rev. C* 96 (2017) 044904. [doi:10.1103/PhysRevC.96.044904](#).
- [35] M. N. Chernodub, Inhomogeneous confining-deconfining phases in rotating plasmas, *Phys. Rev. D* 103 (5) (2021) 054027. [arXiv:2012.04924](#), [doi:10.1103/PhysRevD.103.054027](#).
- [36] S. Wheaton, J. Cleymans, M. Hauer, THERMUS—A thermal model package for ROOT, *Comp. Phys. Comm.* 180 (2009) 84–106. [arXiv:hep-ph/0407174](#), [doi:10.1016/j.cpc.2008.08.001](#).
- [37] W. Rarita, J. Schwinger, On a theory of particles with half integral spin, *Phys. Rev.* 60 (1941) 61. [doi:10.1103/PhysRev.60.61](#).
- [38] G. Velo, D. Zwanziger, Propagation and quantization of Rarita-Schwinger

- waves in an external electromagnetic potential, Phys. Rev. 186 (1969) 1337–1341. doi:[10.1103/PhysRev.186.1337](https://doi.org/10.1103/PhysRev.186.1337).
- [39] K. Johnson, E. C. G. Sudarshan, Inconsistency of the local field theory of charged spin 3/2 particles, Annals Phys. 13 (1961) 126–145. doi:[10.1016/0003-4916\(61\)90030-6](https://doi.org/10.1016/0003-4916(61)90030-6).
- [40] J. Rafelski (Ed.), Melting Hadrons, Boiling Quarks - From Hagedorn Temperature to Ultra-Relativistic Heavy-Ion Collisions at CERN: With a Tribute to Rolf Hagedorn, Springer, 2016. doi:[10.1007/978-3-319-17545-4](https://doi.org/10.1007/978-3-319-17545-4).
- [41] N. Cabibbo, G. Parisi, Exponential Hadronic Spectrum and Quark Liberation, Phys. Lett. B 59 (1975) 67–69. doi:[10.1016/0370-2693\(75\)90158-6](https://doi.org/10.1016/0370-2693(75)90158-6).
- [42] E. Annala, T. Gorda, A. Kurkela, J. Nättilä, A. Vuorinen, Evidence for quark-matter cores in massive neutron stars, Nature Phys. 16 (9) (2020) 907–910. arXiv:[1903.09121](https://arxiv.org/abs/1903.09121), doi:[10.1038/s41567-020-0914-9](https://doi.org/10.1038/s41567-020-0914-9).
- [43] W.-b. He, G.-y. Shao, X.-y. Gao, X.-r. Yang, C.-l. Xie, Speed of sound in QCD matter, Phys. Rev. D 105 (9) (2022) 094024. arXiv:[2205.04614](https://arxiv.org/abs/2205.04614), doi:[10.1103/PhysRevD.105.094024](https://doi.org/10.1103/PhysRevD.105.094024).
- [44] S. Borsanyi, G. Endrodi, Z. Fodor, A. Jakovac, S. D. Katz, S. Krieg, C. Ratti, K. K. Szabo, The QCD equation of state with dynamical quarks, JHEP 11 (2010) 077. arXiv:[1007.2580](https://arxiv.org/abs/1007.2580), doi:[10.1007/JHEP11\(2010\)077](https://doi.org/10.1007/JHEP11(2010)077).
- [45] K. Morita, K. Redlich, [Speed of sound at chiral phase transition](#), quark Matter 2015 - XXV International Conference on Ultrarelativistic Nucleus-Nucleus Collisions (2015).  
URL <https://indico.cern.ch/event/355454/contributions/838638/attachments/1160161/1669963/sound.pdf>
- [46] Y. Aoki, Z. Fodor, S. D. Katz, K. K. Szabo, The QCD transition temperature: Results with physical masses in the continuum limit, Phys. Lett. B 643 (2006) 46–54. arXiv:[hep-lat/0609068](https://arxiv.org/abs/hep-lat/0609068), doi:[10.1016/j.physletb.2006.10.021](https://doi.org/10.1016/j.physletb.2006.10.021).
- [47] M. A. Stephanov, K. Rajagopal, E. V. Shuryak, Signatures of the tricritical point in QCD, Phys. Rev. Lett. 81 (1998) 4816–4819. arXiv:[hep-ph/9806219](https://arxiv.org/abs/hep-ph/9806219), doi:[10.1103/PhysRevLett.81.4816](https://doi.org/10.1103/PhysRevLett.81.4816).
- [48] J. Cleymans, H. Oeschler, K. Redlich, S. Wheaton, [Transition from baryonic to mesonic freeze-out](#), Physics Letters B 615 (1) (2005) 50–54. doi:<https://doi.org/10.1016/j.physletb.2005.03.074>.  
URL <https://www.sciencedirect.com/science/article/pii/S0370269305004211>
- [49] X. Wang, M. Wei, Z. Li, M. Huang, Quark matter under rotation in the NJL model with vector interaction, Phys. Rev. D 99 (1) (2019) 016018. arXiv:[1808.01931](https://arxiv.org/abs/1808.01931), doi:[10.1103/PhysRevD.99.016018](https://doi.org/10.1103/PhysRevD.99.016018).
- [50] M. N. Chernodub, S. Gongyo, Effects of rotation and boundaries on chiral symmetry breaking of relativistic fermions, Phys. Rev. D 95 (9) (2017) 096006. arXiv:[1702.08266](https://arxiv.org/abs/1702.08266), doi:[10.1103/PhysRevD.95.096006](https://doi.org/10.1103/PhysRevD.95.096006).
- [51] K. Fukushima, Y. Hidaka, Magnetic Catalysis Versus Magnetic Inhibition, Phys. Rev. Lett. 110 (3) (2013) 031601. arXiv:[1209.1319](https://arxiv.org/abs/1209.1319), doi:[10.1103/PhysRevLett.110.031601](https://doi.org/10.1103/PhysRevLett.110.031601).
- [52] G. S. Bali, F. Bruckmann, G. Endrodi, Z. Fodor, S. D. Katz, S. Krieg, A. Schafer, K. K. Szabo, The QCD phase diagram for external magnetic fields, JHEP 02 (2012) 044. arXiv:[1111.4956](https://arxiv.org/abs/1111.4956), doi:[10.1007/JHEP02\(2012\)044](https://doi.org/10.1007/JHEP02(2012)044).
- [53] F. Preis, A. Rebhan, A. Schmitt, Inverse magnetic catalysis in field theory and gauge-gravity duality, Lect. Notes Phys. 871 (2013) 51–86. arXiv:[1208.0536](https://arxiv.org/abs/1208.0536), doi:[10.1007/978-3-642-37305-3\\_3](https://doi.org/10.1007/978-3-642-37305-3_3).
- [54] F. Bruckmann, G. Endrodi, T. G. Kovacs, Inverse magnetic catalysis and the Polyakov loop, JHEP 04 (2013) 112. arXiv:[1303.3972](https://arxiv.org/abs/1303.3972), doi:[10.1007/JHEP04\(2013\)112](https://doi.org/10.1007/JHEP04(2013)112).
- [55] N. Sadooghi, S. M. A. Tabatabaee Mehr, F. Taghinavaz, Inverse magnetorotational catalysis and the phase diagram of a rotating hot and magnetized quark matter, Phys. Rev. D 104 (11) (2021) 116022. arXiv:[2108.12760](https://arxiv.org/abs/2108.12760), doi:[10.1103/PhysRevD.104.116022](https://doi.org/10.1103/PhysRevD.104.116022).